Euler Calculations for Wing-Alone Configuration

S. Y. Ruo*
Lockheed-Georgia Company, Marietta, Georgia
and
L. N. Sankar†
Georgia Institute of Technology, Atlanta, Georgia

Steady and unsteady transonic flow over both high- and low-aspect-ratio wings is analyzed through the numerical solution of three-dimensional Euler equations. These equations are solved in a body-fitted coordinate system through a solution procedure that is first-order accurate in time and second-order accurate in space. Wing surface motion is modeled either through a transpiration boundary condition approach or through motion of the body-fitted grid. A number of steady and unsteady flow results are presented and compared with experimental data. The relative merits of the transpiration, and the exact boundary condition approaches are assessed.

Introduction

WITH the availability of supercomputers of the CRAY-XMP class, numerical calculation of the rotational, compressible flow over wings and wing-body configurations has become feasible. In a number of steady flow applications, such as the aerodynamic design of supersonic aircraft wing configurations, the use of Euler solvers has already begun to replace the use of potential flow solvers. In unsteady transonic flow applications, flow solvers based on the extended transonic small-disturbance theory[1-4] and the unsteady full-potential equation[5-7] are not currently considered adequate as a result of the "nonuniqueness" problem with strong shocks. Therefore, there is a need for developing higher-order unsteady flow solvers based on the Euler and Navier-Stokes equations and calibrating them against carefully performed experiments. Such solvers will be needed in the aeroelastic analysis of both past- and present-generation aircraft that operate at Mach numbers and angles of attack at which potential flow assumptions are invalid.

In anticipation of this need for higher-order unsteady transonic flow solvers, a three-dimensional unsteady Euler solver has been developed by the present investigators. The mathematical formulation behind this solver has been described in detail in Refs. 8 and 9, and some comparisons with experimental data for unsteady transonic flow past the F-5 fighter wing and for modern high-speed rotors have also been given.

In this study, the same solution procedure is applied to steady and unsteady transonic flow past thick supercritical wings. Calculations are presented for two supercritical wing configurations, and compared with available experimental data. The first configuration is a large-aspect-ratio supercritical wing tested under the joint sponsorship of Lockheed, the U.S. Air Force, NASA, and National Aerospace Laboratory (NLR).[10] The second configuration is a small-aspect-ratio, thick supercritical wing of rectangular planform tested at the NASA Langley Research Center.[11] Detailed surface pressure comparisons are given for a variety of steady and unsteady flow conditions to determine the suitability of this approach to supercritical wing applications.

In the unsteady flow calculations, the boundary conditions are applied in one of the following two ways. In the first approach, the wing surface and the surrounding body-fitted coordinate system are allowed to move, and the zero normal velocity boundary conditions are applied at the instantaneous boundary surface. In the second approach, the surface motion is simulated at the original, undeformed wing surface through a set of transpiration boundary conditions. Surface pressure distributions at a typical span station computed by the two approaches are compared with experiments to assess the relative merits of the two approaches.

Mathematical Formulation

The mathematical and numerical formulations of the present approach are based on the work reported in Refs. 7-9. A brief description of the governing equations and the discretization formulas used are given in Appendix A. This procedure solves the unsteady, three-dimensional Euler equations in a body-fitted coordinate system. These equations are integrated in time using a finite-difference procedure that is first-order accurate in time, and second-order accurate in space. The solution procedure is fully conservative with respect to the spatial derivatives. The spanwise derivatives are, however, differenced in a manner that is nonconservative with respect to time. The time integration procedure is unconditionally stable from a linear stability analysis. This method requires only one time level of storage. The arithmetic operation count for this method is lower than that for existing alternating-direction-implicit (ADI) schemes, primarily because this method requires only two block tridiagonal matrix inversions per point per time step. This solution procedure has been coded for efficient vectorization on the CRAY-XMP class of computers.

One of the significant improvements in the solution procedure made during this study was the addition of the capability to handle moving grids. The flow over supercritical wing configurations is often very sensitive to subtle changes in the configuration, and the previous version of this solver could handle moving wing surfaces only through a transpiration boundary condition approach. The added capability to account for wing motions exactly and to apply the boundary conditions at the instantaneous boundary exactly allows use of this procedure for large-amplitude surface motions. Comparisons between the exact and the transpiration approaches are

Presented as Paper 87-0108 at the AIAA 25th Aerospace Sciences Meeting, Reno, NV, Jan. 12-15, 1987; received Jan. 20, 1987; revision received Sept. 15, 1987.

*Scientist.

†Associate Professor. Member AIAA.

also possible for identical flow conditions and provide an opportunity for assessing the merits and drawbacks of these two approaches. A brief description of the treatment of the transpiration and the moving grid boundary conditions is given in Appendix B.

The conditions imposed at all the other computational boundaries are discussed in detail for the wing-alone configuration in Refs. 7–9. With minor modifications to the boundary conditions, this solver may also be applied to other configurations, such as wing-body and blended wing-body configurations. In the applications to be discussed below, the body-fitted grid system uses a C-grid topology and was generated algebraically using a sheared parabolic coordinate mapping. In order to better resolve the flow gradients in the direction normal to the wing surface, the C-lines generated by the sheared parabolic mapping were pulled toward the wing surface using an algebraic clustering procedure. In the moving grid calculations, the entire grid was allowed to rotate, and plunge up or down to follow the wing motion.

Results and Discussion

Steady and unsteady transonic flow calculations have been performed for a transport-type supercritical wing configuration, the Lockheed-Air Force-NASA-NLR (LANN) wing, tested at the NLR facilities[10] and for a rectangular supercritical wing tested at the NASA Langley Research Center.[11] A $161 \times 16 \times 21$ grid was used, which has 101 nodes on the airfoil surface at each span station (51 above and 51 below) and 11 span stations. These calculations required roughly 1.55 s for unsteady runs on a CRAY-XMP system per time step. The same time-marching algorithm was used to compute the steady and unsteady flows. Steady calculations required approximately 2000 time steps when a Courant number of the order 20–100 was used. The unsteady calculations were carried out for a sufficient number of cycles (typically three) to ensure that the surface pressures and the integrated loads repeat from cycle to cycle. The solution available during the last cycle was processed to obtain the in-phase (real) and out-of-phase (imaginary) components of the surface pressures and integrated loads. While the in-phase and out-of-phase components of these quantities were extracted, the computed results at time levels corresponding to the 0-, 90-, 180-, and 270-deg phase angles were used. Since the span locations where experimental data are available do not necessarily coincide with the computational span stations, the computed surface pressures were interpolated linearly in the span direction before the computed results were plotted.

The surface pressure distribution may be thought of as the sum of a time-independent mean pressure distribution Cp_o; the first harmonic components often called the in-phase, Cp', and out-of-phase, Cp'', components; and the higher harmonic components. That is,

$$Cp = Cp_o + Cp' \sin(\omega t) + Cp'' \cos(\omega t) + \text{higher harmonics}$$

Steady Flow Analyses

The following steady flow cases are discussed here: a) LANN wing, Mach number 0.62, 0.58-deg angle of attack, b) LANN wing, Mach number 0.82, 0.60-deg angle of attack, c) rectangular supercritical wing, Mach number 0.7, 2-deg angle of attack, and d) rectangular supercritical wing, Mach number 0.86, 7-deg angle of attack. Note that case b is for the design cruise condition of the LANN wing. A number of other calculations for a variety of flow conditions and a few calculations that include viscous corrections have also been carried out. These results are being documented in a separate report.[12]

In Figs. 1–4, the computed surface pressure distributions are plotted and compared with experimental data at four span stations. For convenience, the wing planform is also shown in

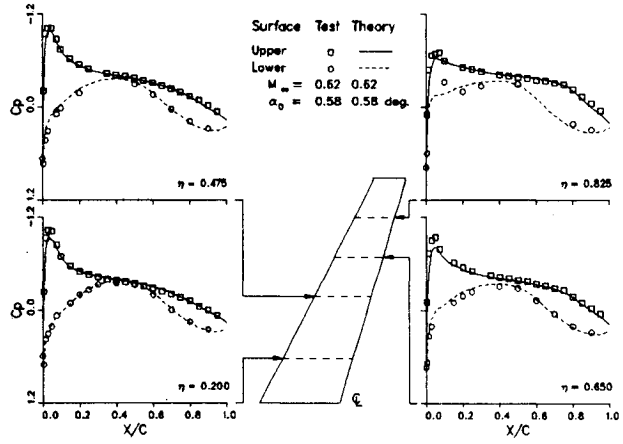

Fig. 1 Steady subcritical pressure distribution over the LANN wing.

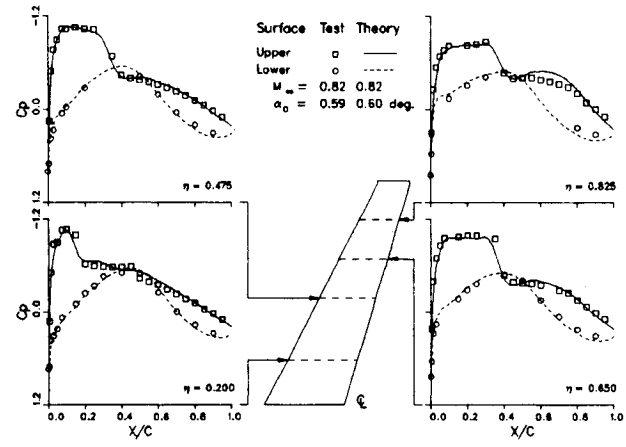

Fig. 2 Steady supercritical pressure distribution over the LANN wing.

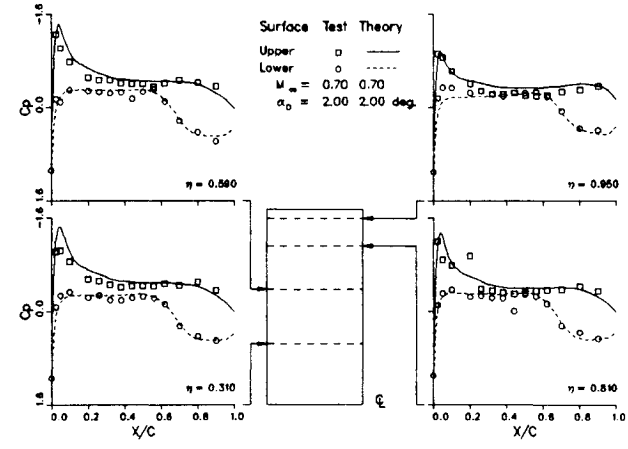

Fig. 3 Steady subcritical pressure distribution over the rectangular wing.

these figures. It is seen that a very good agreement between the theory and the experiment is found in cases a–c. In the case of the rectangular wing at 7-deg angle of attack (case d), good agreement with experiment was found only at the inboard stations, presumably because the flow becomes highly separated in the vicinity of the tip station. The experimental pressure distributions show a plateau near the trailing edge at the tip station, indicating the existence of such a separation. For this case, the freestream Mach number was adjusted from the experimental value of 0.825 to 0.86 in an attempt to correct for any wind tunnel wall or blockage effects at these

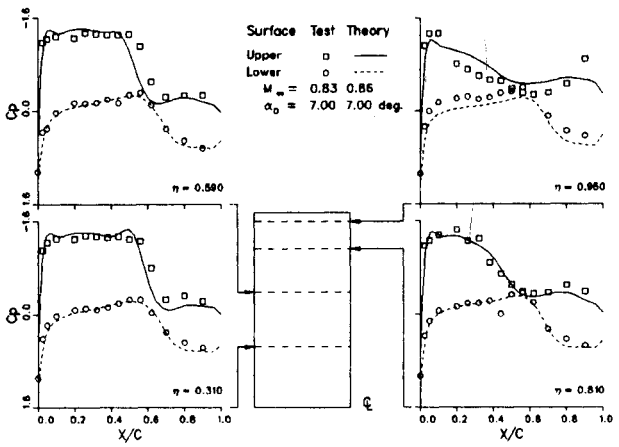

Fig. 4 Steady supercritical pressure distribution over the rectangular wing.

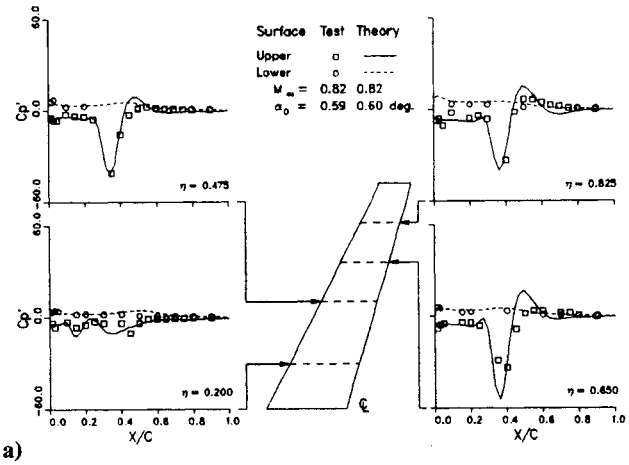

a)

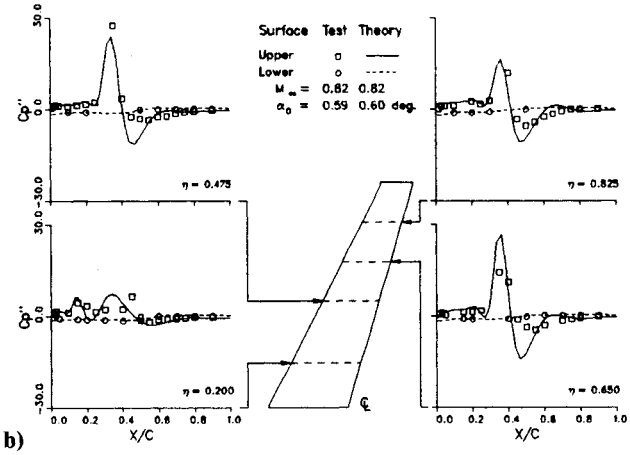

b)

Fig. 5 LANN wing: unsteady pressure distribution, due to pitch at 24 Hz, $k = 0.076$; a) in-phase, b) out-of-phase.

high angles of attack. The experimental studies do not document whether any Mach number or angle of attack corrections will be needed. If the Mach number was set to the actual experimental value of 0.825, a somewhat higher leading-edge suction peak was obtained, and the shock location was approximately 10% forward of the location experimentally observed.

Unsteady Flow Analyses

The following unsteady flow cases are reported in this study: e) LANN wing oscillating in pitch at a frequency of 24 Hz corresponding to a reduced frequency of 0.076 referred to one-half of the mean aerodynamic chord, at 0.82 Mach number and 0.6-deg angle of attack, and f) the rectangular supercritical wing oscillating in pitch at a frequency of 10 Hz corresponding to a reduced frequency of 0.177 referred to one-half of the chord, at 0.7 Mach number and 2-deg angle of attack. A number of additional calculations have been performed and are documented in Ref. 12.

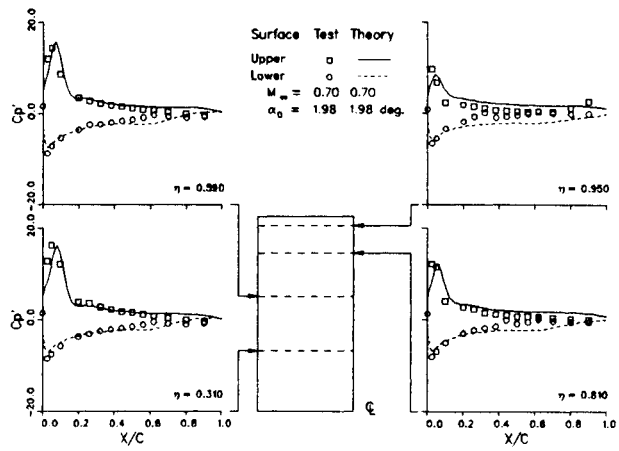

a)

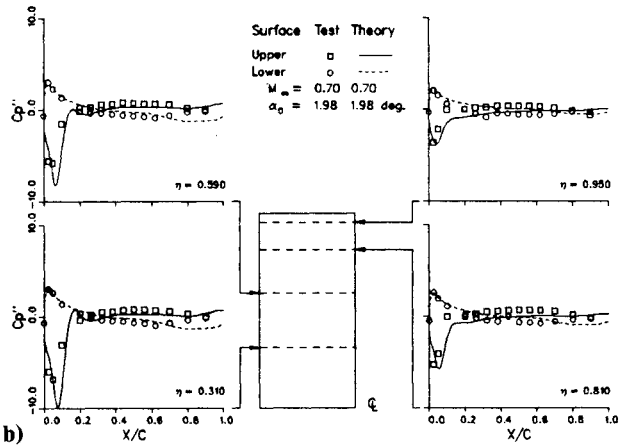

b)

Fig. 6 Rectangular wing: unsteady pressure distribution, due to pitch at 10 Hz, $k = 0.177$; a) in-phase, b) out-of-phase.

In Figs. 5 and 6, the in-phase and the out-of-phase components of the surface pressures using the transpiration boundary condition approach (normalized with the amplitude of oscillations in radians) are shown, and compared with the experimental data. The experimental pressure data at many locations are not considered reliable for the LANN wing case and exceed by a substantial amount the expected values; they are included in these figures only for the sake of completeness. When these out-of-range experimental values are ignored, the theory and the experiment show good agreement both for the in-phase and out-of-phase components. In the case of the rectangular wing, the surface pressure distribution remains predominantly subcritical throughout the cycle. The theory and the experiment tend to agree everywhere except in the vicinity of the tip for the in-phase component of the pressures. This discrepancy may be attributed to the viscous effects that will be dominant only near the tip at this low angle of attack.

The calculations shown in Figs. 5 and 6 were also repeated using the exact boundary condition approach. Comparisons of the unsteady pressure at 59.0% span station obtained from the exact and transpiration boundary condition approaches are shown in Figs. 7 and 8, respectively, for the LANN wing at 47.5% span station and the rectangular wing.

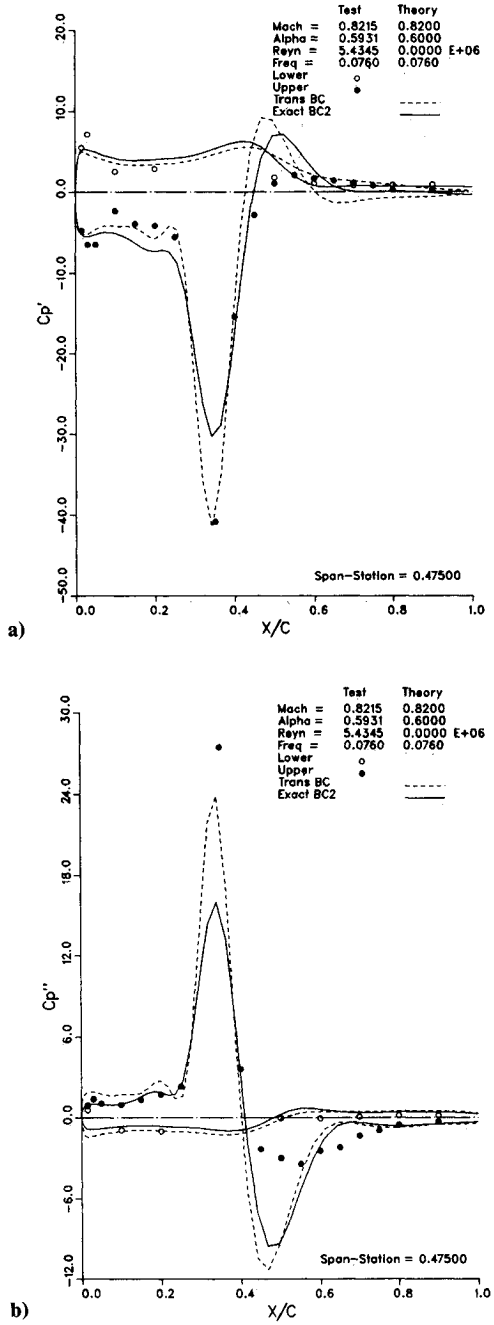

Fig. 7 LANN wing: midspan unsteady pressure using exact and transpiration boundary condition approaches, due to pitch at 24 Hz, $k = 0.076$.

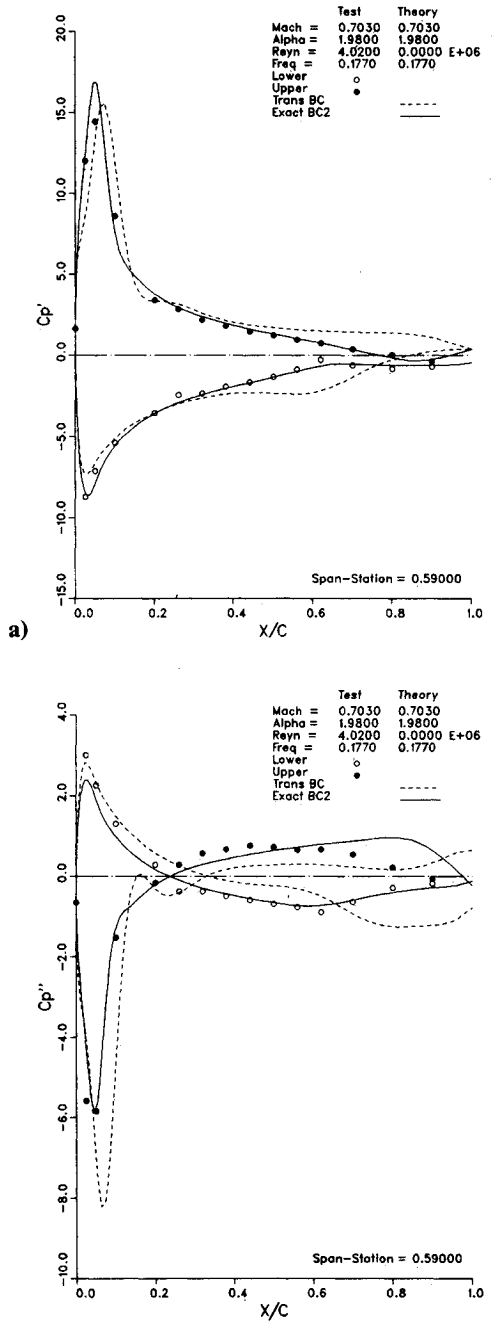

Fig. 8 Rectangular wing: midspan unsteady pressure using exact and transpiration boundary condition approaches, due to pitch at 10 Hz, $k = 0.177$.

For the LANN wing, shown in Fig. 7, it was found that the use of transpiration velocity boundary condition gives a steeper variation of the pressures near shock waves compared to the exact approach. Away from the shocks, the two approaches give virtually similar results. For the subsonic case considered in Fig. 8 for the rectangular wing, the two approaches gave nearly identical results. The exact boundary condition approach tends to capture the rapid pressure variation near the blunt leading edge better than the transpiration approach. The out-of-phase component of the pressures is also better predicted by the exact approach. The exaggerated differences shown in Figs. 7 and 8 are due primarily to the normalization of these pressures by the amplitude of oscillation. In other words, the actual integrated loads for the two approaches will be comparable for the two cases. The trend for the transpiration velocity approach to give a somewhat stronger variation in pressures near shocks has also been observed by other researchers.

In summary, the exact and transpiration approaches yield comparable results for these two cases. The exact boundary condition approach produces results in closer agreement with the experiment for the subsonic case. The transpiration approach tends to produce sharper pressure pulses in the vicinity of the shocks.

The computer times required for the two approaches are closely comparable, as are the computer storage requirements. Thus, for small-amplitude motions of interest to the aeroelastician, either of these approaches is equally suitable. For large-amplitude motions, the exact approach is favorable.

Conclusions

Unsteady and steady transonic rotational flow calculations have been presented for two supercritical wings and have been compared with experiments. Good agreement with experiments was observed for the configurations considered in this study. The issue of exact boundary condition vs transpiration

boundary condition approach was also examined. No clear trend favoring one approach over the other could be found.

Appendix A

The three-dimensional unsteady Euler equations may be written in conservation form in the Cartesian coordinate system as follows:

$$q_t + F_x + G_y + H_z = 0 \tag{A1}$$

where q is the flow properties vector $\{\rho, \rho u, \rho v, \rho w, e\}$, and F, G, and H are the flux vectors along the x, y, and z directions, respectively. For example, F is defined as

$$F = \begin{bmatrix} \rho u \\ \rho u_2 + p \\ \rho uv \\ \rho uw \\ u(e+p) \end{bmatrix} \tag{A2}$$

In the preceding equation set, ρ is the density, and u, v, and w are the flow velocity components along the x, y, and z directions, respectively. Also, e is the total energy per unit volume, and p is the pressure.

The Euler equations were solved in a body-fitted coordinate system (ξ, η, ζ, τ) obtained by first constructing a sheared parabolic coordinate system around the wing and then clustering the C-lines at each span station so that the first C-line off the wing surface is at a constant distance of 0.01 chord from the surface. In this transformed plane, the governing equations become

$$\bar{q}_\tau + \bar{F}_\xi + \bar{G}_\eta + \bar{H}_\zeta = 0 \tag{A3}$$

The quantities $\bar{q}$, $\bar{F}$, $\bar{G}$, and $\bar{H}$ are related to the flow variables $\{q\}$ and the flux vectors in the Cartesian coordinate system through the metrics of transformation. For example,

$$\begin{aligned} \bar{q} &= q/J \\ \bar{F} &= (\xi_t\, q + \xi_x F + \xi_y G + \xi_z H)/J \end{aligned} \tag{A3a}$$

The quantity J is the Jacobian of transformation and is given for the special case in which y is only a function of η by

$$J = \eta_y (\xi_x \zeta_z - \xi_z \zeta_x) \tag{A3b}$$

The unknown in the above system of equations is the flow property vector q. The time derivative of q was discretized using two-point backward differences as $(\delta_\tau\, q)_{n+1}$. The spatial derivatives along the ξ and the η directions were discretized using the following formulas:

$$\begin{aligned} \bar{F}_\xi &= \delta_\xi \bar{F} \\ \bar{H}_\eta &= \delta_\eta \bar{H} \end{aligned} \tag{A4}$$

where δ_ξ and δ_η are three-point central-difference operators. The quantities $\bar{F}$ and $\bar{H}$ are nonlinear functions of $\bar{q}$ at the time level $n+1$. These functions were first linearized about the time level n. For example, $\bar{F}_{n+1}$ was written as follows:

$$\bar{F}^{n+1} = \bar{F}^n + [\mathrm{D}\bar{F}/\mathrm{D}\bar{q}](\bar{q}^{n+1} - \bar{q}^n) \tag{A5}$$

The spanwise derivative $\bar{G}_\eta$ was written as a combination of the n and $n+1$ time levels. During the odd time steps, calculations were done one span station at a time, from the wing root to the outboard span station, using the latest values of the flow vector at the $(n+1)$ time level as soon as they are available. Thus, the quantity $\bar{G}_\eta$ was written at a typical node (i, j, k) as

$$\left(\bar{G}^n_{j+1} - \bar{G}^{n+1}_{j-1}\right)/2$$

During the even time steps, the calculations started at the last span station outboard and progressed until the root station was reached. Then, the term $\bar{G}_\eta$ was discretized as

$$\left(\bar{G}^{n+1}_{j+1} - \bar{G}^n_{j-1}\right)/2$$

Since this differencing uses a mixture of solution vectors at the n and the $(n+1)$ time levels, the procedure is called a hybrid scheme. It may be shown that the use of the values at the $(n+1)$ time level as soon as they are available leads to a stable time-marching scheme from a von Neumann analysis. The reversal of the difference scheme in the spanwise direction from one time step to the next removes any dependence the solution may have on the sweep direction.

The preceding approach has one disadvantage, however. The spanwise derivatives are no longer conservative with respect to time although they are conservative with respect to space. That the spanwise derivatives are nonconservative with respect to time is not expected to affect the solution accuracy since the streamwise and the normal derivatives are all conservatively differenced.

At each of the interior points in the above-mentioned discretization, the following difference equation results for the quantity $(\bar{q}^{n+1} - \bar{q}^n)$:

$$[I + \Delta t \delta_\xi \{\mathrm{D}\bar{F}/\mathrm{D}\bar{q}\}^n + \Delta t \delta_\zeta \{\mathrm{D}\bar{H}/\mathrm{D}\bar{q}\}^n]\,(\bar{q}^{n+1} - \bar{q}^n) = R \tag{A6}$$

where, for the odd time steps, the residual R is given by

$$R = -\Delta t\left[\delta_\xi \bar{F}^n + \delta_\zeta \bar{H}^n + \left(\bar{G}^n_{j+1} - \bar{G}^{n+1}_{j-1}\right)/2\right] \tag{A7}$$

and for the even time steps, the residual is given by

$$R = -\Delta t\left[\delta_\xi \bar{F}^n + \delta_\zeta \bar{H}^n + \left(\bar{G}^{n+1}_{j+1} - \bar{G}^n_{j-1}\right)/2\right] \tag{A8}$$

If pure central differences are used to discretize the spatial derivatives, it may be shown that an odd-even decoupling of the solution occurs after only a few time steps. To prevent this, and in order to remove high-frequency errors from the solution, finite-difference equation (A6) was modified by adding a set of implicit artificial dissipation terms to the residual R:

$$R_1 = -\Delta t \epsilon_E\, [\delta_{\xi\xi\xi\xi} + \delta_{\eta\eta\eta\eta} + \delta_{\zeta\zeta\zeta\zeta}] J \bar{q}^n \tag{A9}$$

To the left-hand side operator of Eq. (A6), the following implicit dissipation operators were added:

$$-\Delta t \epsilon_I J^{-1} (\delta_{\xi\xi} + \delta_{\zeta\zeta})\, J \tag{A10}$$

The constants ϵ_E and ϵ_I are user input coefficients. Typically, these two coefficients were set equal to 1 and 3, respectively.

After the preceding dissipation terms were added, the left-hand side operator appearing in Eq. (A6) was approximately factored into a product of two one-dimensional operators, resulting in the following equation:

$$\begin{aligned} &[I + \Delta t \delta_\xi \{\mathrm{D}\bar{F}/\mathrm{D}\bar{q}\} - \Delta t \epsilon_I J^{-1} \delta_{\xi\xi} J] \times \\ &[I + \Delta t \delta_\zeta \{\mathrm{D}\bar{H}/\mathrm{D}\bar{q}\} - \Delta t \epsilon_I J^{-1} \delta_{\zeta\zeta} J] \times \\ &(\Delta \bar{q}^{n+1}) = R + R_1 \end{aligned} \tag{A11}$$

where $\Delta \bar{q}^{n+1} = \bar{q}^{n+1} - \bar{q}^n$

This factored equation was solved using a series of block tridiagonal matrix inversions. The values of $\Delta\bar{q}$ at the computational boundaries were set to zero. The flow property vector q at these boundaries was updated after the interior points were updated.

Appendix B

Appendix B briefly describes the treatment of grid motion, as well as transpiration boundary conditions.

Grid Motion

For the supercritical wings considered here, the surface motion at a given span station may arise from both torsional and bending deformations. A line exists (often called the node line) that runs from the root of the wing to the tip, along which the deflections are zero. The shape of the node line and the amplitude of the sinusoidal pitching and bending deformations at each span station with reference to the node line are known from experimental measurement and are input into the computer code as a table of x_0, y_0, θ_0, and h_0 values, where (x_0, y_0,) define the shape of the node line and θ_0 and h_0 are the amplitude of the sinusoidal pitching and plunging motions. These values were linearly interpolated to obtain x_0, θ_0, and h_0 values at the computational spanwise locations.

At any time level t, the pitching and bending deflections with respect to the node line θ and h may now be computed as

$$\theta = \theta_0 \sin(\omega t)$$

$$h = h_0 \sin(\omega t) \tag{B1}$$

Knowing θ and h at a given span station at a time level t, the instantaneous grid (x, y, z) may be computed in terms of the original rigid grid ($\bar{x}$, $\bar{y}$, $\bar{z}$) as

$$y = \bar{y}$$

$$x = x_0 + (\bar{x} - x_0)\cos(\theta) - \bar{z}\sin(\theta)$$

$$z = h + (\bar{x} - x_0)\sin(\theta) + \bar{z}\cos(\theta) \tag{B2}$$

In the moving grid case, the grid was redefined at every time step using Eq. (B2). The grid velocities $\dot{x}$, $\dot{y}$, $\dot{z}$ were computed as the analytical derivatives of the expressions given in Eq. (B2). An alternate form of computing $\dot{x}$ as $[x(t+\Delta t) - x(t)]/(\Delta t)$ has also been considered with success.

Boundary Conditions at Solid Surface

The boundary conditions used at the solid surface are as follows. The density and pressure values have been extrapolated from the interior as follows:

$$\frac{\partial \rho}{\partial n} = 0; \qquad \frac{\partial p}{\partial n} = 0 \tag{B3}$$

where n denotes the normal distance from the solid surface. A slightly more accurate boundary condition for pressure would include pressure relief at the solid surface due to centrifugal effects. This approach has not been tested by the present researchers.

The two tangential components of velocity along the streamwise and spanwise directions were extrapolated from the interior. This was done by satisfying at a node (i, j, 1) on the solid surface the following relationships. Let U_{ij1} and V_{ij1} be contravariant components of velocity given by

$$U_{ij1} = [(u - x_\tau)\xi_x + (v - y_\tau)\xi_y + (w - z_\tau)\xi_z]$$

$$V_{ij1} = [(u - x_\tau)\eta_x + (v - y_\tau)\eta_y + (w - z_\tau)\eta_z] \tag{B4}$$

These values are computed as

$$U_{ij1} = 2\,U_{ij2} - U_{ij3}$$

$$V_{ij1} = 2\,V_{ij2} - V_{ij3} \tag{B5}$$

These give two relationships for the three Cartesian components of velocity u, v, and w.

The exact and the transpiration velocity boundary condition approaches differ from each other in how the normal boundary condition was applied. This boundary condition, often called the zero normal velocity condition, requires that the fluid and the solid have the same normal velocity at the solid surface. That is,

$$(u - x_\tau)\zeta_x + (v - y_\tau)\zeta_y + (w - z_\tau)\zeta_z = 0 \tag{B6}$$

In the exact boundary condition approach, Eq. (B6) was satisfied at each time step in conjunction with Eq. (B5), using the most recent metric terms computed for the deformed grid.

In the transpiration boundary condition approach, the metrics are not recomputed at every time step. Thus, the metrics do not have any information about the local changes in the body slope from one time step to the next and would yield incorrect results if they are used in Eq. (B6).

To account for the local changes in body slope from one time step to the next, it is necessary either to recompute the metrics at every time step, at least on the body surface, or to account for it in the following manner:

$$(u - x_\tau)\zeta_x + (v - y_\tau)\zeta_y + (w - z_\tau)\zeta_z = \left[\frac{\mathrm{d}}{\mathrm{d}x}(\Delta z)\right]\zeta_z \tag{B7}$$

where Δz is the difference in the z coordinate between the rigid grid and the deformed grid at each time step on the surface. Equation (B7) closely resembles Eq. (B6), except that the right-hand side is nonzero. In the present work, this nonzero velocity component is called "transpiration" velocity.

References

[1]Edwards, J. W., Bland, S. R., and Seidel, D. A., "Experience with Transonic Unsteady Aerodynamic Calculations," NASA TM 86278, Aug. 1984; also "Transonic Unsteady Aerodynamics and its Aeroelastic Applications," AGARD-CP-374, Jan. 1985.

[2]Bennett, R. M., Seidel, D. A., and Sandford, M. C., "Transonic Calculations for a Flexible Supercritical Wing and Comparison with Experiment," AIAA Paper 85-0665, April 1985.

[3]Batina, J. T., "Unsteady Transonic Flow Calculations for Wing-Fuselage Configurations," AIAA Paper 86-0862, May 1986.

[4]Guruswamy, G. P., Goorjian, P. M., and Tu, E. L., "Unsteady Transonics of a Wing with Tip Store," *Journal of Aircraft*, Vol. 23, Aug. 1986, pp. 662–668.

[5]Shankar, V. and Ide, H., "Treatment of Steady and Unsteady Flows Using a Fast, Time-Accurate Full Potential Scheme," AIAA Paper 85-4060, Oct. 1985.

[6]Malone, J. B. and Sankar, L. N., "Unsteady Full Potential Calculations for Complex Wing-Body Configurations," AIAA Paper 85-4062, Oct. 1985.

[7]Ruo, S. Y., Malone, J. B., and Sankar, L. N., "Steady and Unsteady Full Potential Calculations for High and Low Aspect Ratio Supercritical Wings,"AIAA Paper 86-0122, Jan. 1986.

[8]Sankar, L. N., Wake, B. E., and Lekoudis, S. G., "Solution of the Unsteady Euler Equations for Fixed and Rotary Wing Configurations," AIAA Paper 85-0120, 1985.

[9]Sankar, L. N., Malone, J. B., and Schuster, D., "Full Potential and Euler Solutions for the Unsteady Flow Past a Fighter Wing,"AIAA Paper 85-4061, 1985.

[10]Ruo, S. Y., Malone, J. B., Horsten, J. J., and Houwink, R., "The LANN Program: An Experimental and Theoretical Study of Steady and Unsteady Transonic Airloads on a Supercritical Wing," AIAA Paper 83-1636, 1983.

[11]Ricketts, R. H., Sandford, M. C., Watson, J. J., and Seidel, D. A., "Subsonic and Transonic Unsteady- and Steady-Pressure Measurements on a Rectangular Supercritical Wing Oscillated in Pitch," NASA TM-85765, Aug. 1984.

[12]Ruo, S. Y. and Sankar, L. N., "Numerical Study of Unsteady Rotational Flow over Wing-Alone Configurations," Lockheed-Georgia Co., Marietta, GA, Rept. LG86ER0178, July 1987.